

Variational Quantum Algorithm for Constrained Topology Optimization in Quantum Scientific Computing

Jungin E. Kim¹, Jinhwan Sul¹, and Yan Wang¹

¹Georgia Institute of Technology, Atlanta, GA 30332, USA

December 9, 2024

Abstract

Quantum scientific computing has emerged as a new paradigm to solve difficult scientific computing problems on quantum computers. One of them is topology optimization, which is computationally expensive because the combinatorial optimization problem and partial differential equations need to be solved simultaneously. In this paper, we propose a novel variational quantum algorithm for topology optimization through quantum entanglement. Two quantum registers are used to encode the optimal configurations and the solutions to physical constraints, respectively. The tasks of finding the optimal material configuration and solving the physical constraints are performed simultaneously in a single loop. A constraint encoding scheme is also proposed to incorporate volume and topology constraints in optimization. The gate complexity of the proposed quantum algorithm is analyzed. The theoretical lower bound of the success probability is obtained. The algorithm is demonstrated with compliance minimization problems including truss structures and Messerschmitt-Bölkow-Blohm beams.

1. Introduction

Topology optimization (TO) is the process of finding the optimal material configuration of a structure to achieve some desirable properties [1]. It has a wide variety of applications, such as microfluidic reactors [2], photonic crystals [3], topological insulators [4], cloaking [5], acoustic barriers [6], lightweight structures [7], multi-material composites [8], and many more. However, solving TO problems is challenging for two reasons. First, searching through a combinatorially large number of possible configurations is expensive. Second, the evaluation of design objective for each configuration requires solving partial differential equations (PDEs) to obtain the quantities of interest and often relies on expensive simulations. Therefore, computational efficiency remains a major challenge in TO. In the past decade, quantum scientific computing has emerged as a new paradigm to solve difficult scientific computing problems on quantum computers, such as engineering simulation [9, 10], optimization [11, 12], materials design [13, 14], drug discovery [15], and others. It has the potential to significantly improve the efficiency of TO, because each quantum basis state can naturally encode a configuration in the exponentially large design solution space [12].

Recently, both quantum annealers and circuit-based quantum computers started being used to solve TO problems. In quantum annealing [16], problems are formulated as quadratic unconstrained binary optimization (QUBO). The quantum system is perturbed in order to transition from the initial state to the target ground state, utilizing the adiabatic quantum computation scheme [17]. The ground state represents the optimal solution. Ye et al. [18] decomposed TO problems into sequences of mixed-integer nonlinear programs, where each problem is reformulated as QUBO. Honda et al. [19] optimized the topology of two- and three-dimensional truss structures, where the nodal displacements are expressed as binary strings. Although QUBO formulations allow quantum annealing to be applied to encode material configurations efficiently, the PDE constraints in TO involve continuous variables and impose the challenge of binary representation to quantum annealers. Among the circuit-based computational approaches, variational quantum algorithms (VQAs) such as quantum approximate optimization algorithm (QAOA) [20, 21] and variational quantum eigensolver [22] are the most suitable ones to solve real-world problems on near-term quantum computers. In this hybrid quantum-classical approach, computation is

performed by evolving the quantum state through parameterized quantum gates. The parameters are optimized by classical optimizers iteratively in the outer loop. VQAs have been used to solve TO problems. Kim and Wang [23] applied a quantum approximate Bayesian optimization algorithm [24] to perform TO for trusses and metamaterials, where a surrogate-based global optimizer, Bayesian optimization, is used to train the parameters of the variational quantum circuit. Sato et al. [25] proposed a double-loop optimization framework which involves two quantum circuits. The first circuit is used to solve the PDE constraints for all possible configurations. The second circuit is to maximize the probability of obtaining the optimal configuration.

In this paper, we propose a new VQA to solve TO problems efficiently through quantum entanglement. Two quantum registers are used to encode the two types of values in TO, respectively. The first type is the optimal configuration as the solution of TO, whereas the second one represents physical quantities which satisfy the PDE constraints. Two entanglement mechanisms are introduced to compute both values concurrently. First, the problem Hamiltonian operators corresponding to the PDE constraints in the VQA circuit are entangled with the first register. Second, the qubits in the second register are also entangled to improve the searching efficiency and reduce the circuit depth. Furthermore, a constraint encoding scheme is also proposed to incorporate topology and volume constraints of the optimization problems as constraints of VQA parameters.

Researchers have developed approaches to incorporate constraints in quantum optimization. The most common approach is to incorporate constraints as the regularization or penalty terms in the objective function. The problem Hamiltonian is subsequently altered, and the ground state corresponds to the optimal solution which is likely to satisfy the constraints. This approach is for problems involving soft constraints. For instance, Hen and Sarandy [26] formulated the Hamiltonian as the sum of the original Hamiltonian and the operators that encode the constraints. Fernández-Lorenzo et al. [27] used the variational quantum eigensolver and QAOA to find the ground state of an Ising Hamiltonian which represents the Lagrangian of a QUBO problem. Djidjev [28] used quantum annealing to minimize a sum of objective, constraint, and the squared constraint functions. Montañez-Barrera et al. [29] solved QUBO problems with quantum annealing and QAOA, where the constraint penalty term is formulated as an exponential function. The second approach to incorporate constraints is to design quantum operators that only search within the feasible solution space. For QAOA, this is achieved by designing the mixing Hamiltonians. One example is the XY mixing Hamiltonian which restricts the feasible basis states on a graph [30, 31]. The second example is to design the mixing Hamiltonian in QAOA or the driver Hamiltonian for quantum annealing such that it commutes with the operators associated with linear constraints [32]. A third instance is a continuous-time quantum walk operator [33, 34] where a graph adjacency matrix restricts the search process. The third approach to incorporate constraints in quantum optimization is to treat objective and constraints separately and formulate the problems as multi-objective optimization. Díez-Valle et al. [35] proposed VQAs to solve the objective minimization and constraint satisfaction problems simultaneously. The proposed constraint encoding scheme here is different from the existing approaches. The design constraints are mapped to the constraints of the parameters in the variational quantum circuit. Particularly, the volume constraints in TO are enforced by setting an upper bound for the parameters of the uncontrolled rotation gates, whereas the topological constraints are encoded in the controlled rotation gates such that the amplitudes of infeasible configurations are minimized.

The remainder of the paper is structured as follows. In Section , the proposed TO formalism is introduced. In Section , the quantum circuit which encodes the topological and volume constraints is described. In Section , the success probability of the proposed VQA is analyzed. In Section , the proposed TO approach is demonstrated with five examples. The first three examples involves minimizing the compliance of truss structures, whereas the other two examples are about minimizing the compliance of a Messerschmitt-Bölkow-Blohm (MBB) beam. Discussions and conclusions are provided in Section .

2. Proposed Variational Quantum Topology Optimization Algorithm

In TO problems, the spatial domain is typically discretized as elements. Choosing the material configuration is equivalent to choosing a subset of elements so that the best objective value is obtained. The proposed VQA performs the tasks of finding the optimal material configuration and solving the PDE constraints simultaneously. The parameterized quantum circuit includes two registers. The first register

encodes the material configurations, whereas the second one encodes the PDE solutions. Each PDE solution is entangled with the corresponding material configuration. This is done through a controlled problem Hamiltonian operator, which is implemented with a sequence of controlled operators applied on the second register. In addition, an alternating sequence of rotation and CNOT gates are applied on the second register. The entanglement between the qubits reduces the size of the searching space and the circuit depth.

2.1. Problem Hamiltonian Formulation

Without the loss of generality, here the truss compliance minimization problem is used to illustrate the formulation of problem Hamiltonians. The compliance minimization problem for truss structure design is typically formulated as

$$\begin{aligned} \min_{\mathbf{q}, \mathbf{u}} \quad & \mathbf{u}^\top K(\mathbf{q})\mathbf{u} \\ \text{s.t.} \quad & K(\mathbf{q})\mathbf{u} = \tilde{\mathbf{f}}, \end{aligned} \quad (1)$$

where $\mathbf{u} \in \mathbb{R}^N$ is the displacement vector, N is the number of degrees of freedom, \mathbf{q} is the material configuration, $K(\mathbf{q}) \in \mathbb{R}^{N \times N}$ is the total stiffness matrix of the structure which depends on configuration \mathbf{q} , and $\tilde{\mathbf{f}} \in \mathbb{R}^N$ is the load vector. The linear constraint in Eq. (1) is obtained from the weak form of PDEs in the finite-element formulation. In the VQA, the discrete variable of material configurations \mathbf{q} is encoded as the state of the first quantum register, whereas the displacement vector \mathbf{u} is encoded as the amplitudes of the second register.

In a double-loop TO process, the constraint in Eq. (1) is solved in the inner loop, whereas the optimization is performed in the outer loop. To solve the problem in a single-loop TO process, the constraint in Eq. (1) needs to be combined into the objective as the regularization term. It is important to obtain a quadratic form of objective function so that the Hamiltonian can be constructed. Therefore, the compliance minimization problem is reformulated as

$$\begin{aligned} \min_{\mathbf{q}, \mathbf{u}, \mathbf{f}, \alpha} \quad & \mathbf{u}^\top K(\mathbf{q})\mathbf{u} + \lambda \|K(\mathbf{q})\mathbf{u} - \alpha\mathbf{f}\|^2 \\ \text{s.t.} \quad & \alpha\mathbf{f} = \tilde{\mathbf{f}} \end{aligned} \quad (2)$$

where $\mathbf{f} \in \mathbb{R}^N$ is a vector of variables corresponding to the estimated loads, $\lambda \in \mathbb{R}^+$ is a Lagrange multiplier, and $\alpha \in \mathbb{R}^+$ is a scaling factor. α must be included so that \mathbf{f} is scaled to $\tilde{\mathbf{f}}$ (i.e. $\|\alpha\mathbf{f}\| = \|\tilde{\mathbf{f}}\|$).

With \mathbf{f} introduced into the problem in Eq. (2), the objective function is now strictly quadratic with respect to $\mathbf{w} = [\mathbf{u}^\top \quad -\mathbf{f}^\top]^\top$, because

$$\mathbf{u}^\top K(\mathbf{q})\mathbf{u} = [\mathbf{u}^\top \quad -\mathbf{f}^\top] \begin{bmatrix} K(\mathbf{q}) & \mathbf{0} \\ \mathbf{0} & \mathbf{0} \end{bmatrix} \begin{bmatrix} \mathbf{u} \\ -\mathbf{f} \end{bmatrix} \quad (3)$$

and

$$\|K(\mathbf{q})\mathbf{u} - \alpha\mathbf{f}\|^2 = [\mathbf{u}^\top \quad -\mathbf{f}^\top] \begin{bmatrix} K^2(\mathbf{q}) & \alpha K(\mathbf{q}) \\ \alpha K(\mathbf{q}) & \alpha^2 I \end{bmatrix} \begin{bmatrix} \mathbf{u} \\ -\mathbf{f} \end{bmatrix}. \quad (4)$$

Let

$$A(\mathbf{q}) = \begin{bmatrix} K(\mathbf{q}) & \mathbf{0} \\ \mathbf{0} & I \end{bmatrix} \in \mathbb{R}^{2N \times 2N} \quad (5)$$

and

$$B(\mathbf{q}, \alpha) = \begin{bmatrix} K^2(\mathbf{q}) & \alpha K(\mathbf{q}) \\ \alpha K(\mathbf{q}) & \alpha^2 I \end{bmatrix} \in \mathbb{R}^{2N \times 2N}. \quad (6)$$

The minimization problem subsequently becomes

$$\begin{aligned} \min_{\mathbf{q}, \mathbf{w}, \alpha} \quad & \mathbf{w}^\top (A(\mathbf{q}) + \lambda B(\mathbf{q}, \alpha)) \mathbf{w} \\ \text{s.t.} \quad & \alpha\mathbf{f} = \tilde{\mathbf{f}}, \end{aligned} \quad (7)$$

where the objective function resembles the expected value of the Hamiltonian with respect to \mathbf{w} . Therefore, the problem Hamiltonian is defined as

$$\mathcal{H}(\mathbf{q}, \alpha) = A(\mathbf{q}) + \lambda B(\mathbf{q}, \alpha) = \begin{bmatrix} K + \lambda K^2 & \lambda \alpha K \\ \lambda \alpha K & \lambda \alpha^2 I \end{bmatrix} \quad (8)$$

so that the minimum expected objective value is associated with the optimal configuration and displacements. It is noted that $\mathcal{H}(\mathbf{q}, \alpha)$ is symmetric and positive semi-definite, since $K(\mathbf{q})$ is symmetric and the objective values in Eq. (2) are non-negative.

The compliance minimization problem in Eq. (7) can be further reformulated as

$$\min_{\mathbf{q}, \mathbf{w}, \alpha} \mathbf{w}^\top \mathcal{H}(\mathbf{q}, \alpha) \mathbf{w} + \mu \|\alpha \mathbf{f} - \tilde{\mathbf{f}}\|^2, \quad (9)$$

where $\mu \in \mathbb{R}^+$ is another Lagrange multiplier. The first term in Eq. (9) is computed on quantum computer. The second term is computed on classical computer, since it does not have a quadratic form and a corresponding Hamiltonian is not available.

2.2. Controlled Problem Hamiltonian Operator

The core operator is the problem Hamiltonian operator $U_C(\gamma, \mathbf{q}, \alpha)$, which is applied to the second register that encodes \mathbf{w} . Since the problem Hamiltonian depends on the material configuration \mathbf{q} , it is controlled by the first register. The control scheme is derived based on the decomposition of $K(\mathbf{q})$ and the Trotter-Suzuki approximation [36]. Let

$$K(\mathbf{q}) = K_0 + \sum_{j=1}^m q_j K_j, \quad (10)$$

where K_0 is the stiffness matrix of the base structure without optional elements, and K_j 's are stiffness matrices associated with the m optional elements ($j = 1, \dots, m$). q_j is a binary variable which indicates the presence or absence of the j^{th} optional element.

For simplicity of notation, let

$$Q^{(0)}(\alpha) = \begin{bmatrix} K_0 + \lambda K_0^2 & \alpha \lambda K_0 \\ \alpha \lambda K_0 & \alpha^2 \lambda I \end{bmatrix}, \quad (11)$$

$$Q^{(1)}(q_j, \alpha) = q_j \begin{bmatrix} K_j + \lambda K_0 K_j + \lambda K_j K_0 + \lambda K_j^2 & \alpha \lambda K_j \\ \alpha \lambda K_j & \mathbf{0} \end{bmatrix}, \quad (12)$$

and

$$Q^{(2)}(q_j, q_k) = q_j q_k \begin{bmatrix} \lambda(K_j K_k + K_k K_j) & \mathbf{0} \\ \mathbf{0} & \mathbf{0} \end{bmatrix}. \quad (13)$$

With the Trotter-Suzuki approximation, U_C becomes

$$U_C(\gamma, \mathbf{q}, \alpha) \approx e^{-i\gamma Q^{(0)}(\cdot)} \left[\prod_{j=1}^m e^{-i\gamma Q^{(1)}(\cdot)} \right] \left[\prod_{j=1}^{m-1} \prod_{k=j+1}^m e^{-i\gamma Q^{(2)}(\cdot)} \right], \quad (14)$$

where γ is a rotation parameter.

The problem Hamiltonian operator in Eq. (14) is a product of three terms. The first term, $\exp(-i\gamma Q^{(0)}(\alpha))$, is independent of \mathbf{q} . The second term, $\prod_{j=1}^m \exp(-i\gamma Q^{(1)}(q_j, \alpha))$, is a product of unitary operators, each of which is associated with one optional element q_j . The third term, $\prod_{j=1}^{m-1} \prod_{k=j+1}^m \exp(-i\gamma Q^{(2)}(q_j, q_k))$, is also a product of unitary operators, and each one is associated with two optional elements q_j and q_k . $U_C(\gamma, \mathbf{q}, \alpha)$ is a combination of operators corresponding to the present elements.

The application of $U_C(\gamma, \mathbf{q}, \alpha)$ on the second register is controlled by the first register. The quantum state of the second register that encodes the displacements is entangled with the one of the first register which indicates the topology. As a result, the tasks of minimizing the compliance and solving the PDE constraints can be performed simultaneously.

2.3. Gate Complexity of Problem Hamiltonian Operator

The control problem Hamiltonian operator is comprised of one $Q^{(0)}$, m of $Q^{(1)}$, and $m(m-1)/2$ of $Q^{(2)}$. Each Hermitian operator $Q^{(\cdot)}$ is decomposed as

$$Q^{(\cdot)} = \sum_{j=1}^D c_j \sigma_j, \quad (15)$$

where D is the number of Pauli operator terms, σ_j is a tensor product of Pauli operators, and $c_j \in \mathbb{C}$ is the coefficient of σ_j . The value of D depends on the sparsity of $Q^{(\cdot)}$. The following theorem establishes an upper bound for D .

Theorem 1 ([37]). *Suppose $Q^{(\cdot)}$ is a d -sparse Hermitian matrix. Then*

$$D \leq 4d^2 \left\lceil \log_2 \left(2^{1/2} \|Q^{(\cdot)}\|_{\max} \right) \right\rceil \quad (16)$$

where $\|Q^{(\cdot)}\|_{\max}$ is the maximum absolute value of any entry in $Q^{(\cdot)}$.

The sparsity depends on each type of $Q^{(\cdot)}$. Let v be the maximum number of elements connected to a single node in a truss structure. For $Q^{(0)}$, the largest value of d is $4v$ since the base structure can contain elements which connect between one node and all other nodes. For $Q^{(1)}$, the largest value of d is $2v + 4$ since K_0 only appears in the top-left submatrix of $Q^{(1)}$ and each K_j has at most four non-zero entries in a row or column. For $Q^{(2)}$, the largest value of d is 6 since the two optional elements associated with $Q^{(2)}$ can share the same node.

With the Trotter-Suzuki approximation, the operator $e^{-i\gamma Q}$ is approximated as

$$e^{-i\gamma Q} \approx \prod_{j=1}^D e^{-i\gamma c_j \sigma_j}. \quad (17)$$

Each $e^{-i\gamma c_j \sigma_j}$ is implemented with up to one Z-rotation gate, $2(n-1)$ CNOT gates, and $2n$ gates which convert any Pauli-X and Pauli-Y operators into Pauli-Z operators.

Overall, U_C consists of $\mathcal{O}(nv^2 \lceil \log_2(2^{1/2} \|Q^{(0)}\|_{\max}) \rceil)$ quantum gates for $Q^{(0)}$, $\mathcal{O}(nv^2 \lceil \log_2(2^{1/2} \|Q^{(1)}\|_{\max}) \rceil)$ gates for each $Q^{(1)}$, and $\mathcal{O}(n \lceil \log_2(2^{1/2} \|Q^{(2)}\|_{\max}) \rceil)$ gates for each $Q^{(2)}$. The gate complexity of U_C depends on the arrangement of elements in the structure. As the number of elements connected to a single node decreases, the sparsity of the stiffness matrices increases. As a result, fewer quantum gates are needed to construct the control scheme.

2.4. Quantum Circuit Architecture

The overall quantum circuit for the proposed VQA is shown in Figure 1. In the first register $|q\rangle = \otimes_{j=1}^m |q_j\rangle$, the computational basis encodes a total of 2^m material configurations. In the second register $|w\rangle = \otimes_{j=1}^n |w_j\rangle$, the amplitudes of $n = \lceil \log_2 N \rceil + 1$ qubits represent the estimated displacements \mathbf{u} and loads \mathbf{f} collectively. All qubits are initialized as $|0\rangle$.

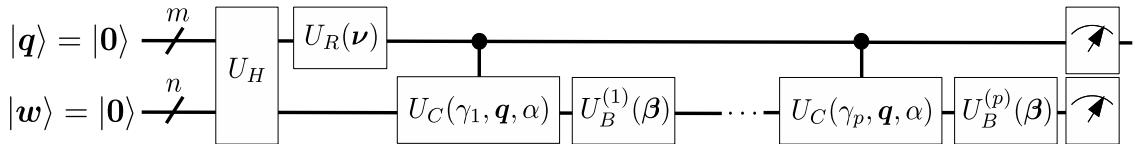


Figure 1: The architecture of the proposed variational quantum topology optimization algorithm

The overall operator is defined as

$$W = [(I \otimes U_B)W_C]^p (U_R \otimes I)U_H, \quad (18)$$

where p is the number of repetitions. U_H is the Walsh-Hadamard transform, defined as

$$U_H = H^{\otimes(m+n)}. \quad (19)$$

U_R is defined as

$$U_R(\boldsymbol{\nu}) = \otimes_{j=1}^m e^{-i\nu_j \sigma_X}, \quad (20)$$

where ν_j 's are parameters and σ_X is the Pauli-X matrix. W_C is defined as

$$W_C(\gamma, \mathbf{q}, \alpha) = \sum_{\mathbf{q} \in \{0,1\}^m} |\mathbf{q}\rangle\langle \mathbf{q}| \otimes U_C(\gamma, \mathbf{q}, \alpha). \quad (21)$$

U_B is defined as

$$U_B(\boldsymbol{\beta}) = (|0\rangle\langle 0|I + |1\rangle\langle 1|\sigma_X)^{\otimes (\lfloor n/2 \rfloor)} \left(\otimes_{k=1}^n e^{-i\beta_k \sigma_X} \right), \quad (22)$$

where β_k 's are parameters.

The application of U_R on $|\mathbf{q}\rangle$ results in the exploration of all material configurations. Therefore, the quantum circuit is applicable for unconstrained TO problems. For constrained TO problems, an alternative rotation operator which explores feasible configurations is needed.

3. Constraint Encoding

To solve constrained TO problems, a sequence of controlled and uncontrolled rotation gates \tilde{U}_R are applied on $|\mathbf{q}\rangle$ instead of U_R described in the previous section. This sequence is defined as

$$\tilde{U}_R(\xi, \boldsymbol{\nu}) = U_T(\xi)U_R(\boldsymbol{\nu}), \quad (23)$$

where $\xi \in \mathbb{R}^-$ is a rotation parameter and U_T is a sequence of controlled rotation gates. Each rotation gate is applied to a qubit about the x-axis in the Bloch sphere. By applying the rotation gates and restricting the ranges of parameters, the search space is reduced to feasible configurations which satisfy the constraints.

Two types of constraints are encoded. The first type is topological constraint, which ensures that elements in the structure are connected with each other. A configuration which satisfies topological constraints does not contain the checkerboard patterns or elements which are located in the centers of voids. The topological constraints are encoded with the controlled rotation gates. To illustrate, let q_j and q_k denote the presence of two adjacent optional elements. For example, when $q_k = 1$, it is required that $q_j = 1$ so that the optional elements are connected to the base structure. A controlled rotation gate is applied where $|q_j\rangle$ is the control qubit and $|q_k\rangle$ is the target qubit. When $|q_j\rangle = |0\rangle$, the gate decreases the amplitude of $|1\rangle$ in $|q_k\rangle$. As a result, the probability of measuring structures where $q_j = 0$ and $q_k = 1$ decreases. Figure 2 shows an example of \tilde{U}_R , which encodes the constraint that $q_4 = 0$ when both $q_2 = 0$ and $q_3 = 0$. In this case, the rotation gate applied on $|q_4\rangle$ is controlled by both $|q_2\rangle$ and $|q_3\rangle$. The rotation is only performed when both $|q_2\rangle = |0\rangle$ and $|q_3\rangle = |0\rangle$.

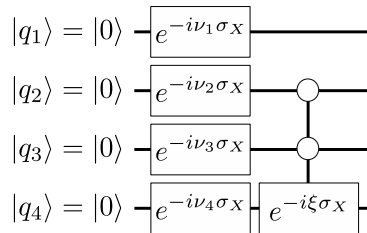


Figure 2: An example of topological constraints encoded in \tilde{U}_R

The second type is a volume constraint, which limits the maximum number of included elements. The volume constraints are encoded by setting an upper bound ν^* for ν_j 's, as $\nu_j \leq \nu^*$. By enforcing this constraint, some of the qubits are likely to be measured as $|1\rangle$, whereas the other qubits are likely to be measured as $|0\rangle$. In general, as ν^* increases, the probability of including more elements in the optimal configuration increases. The following theorem establishes the guidance of choosing the maximum value ν^* .

Theorem 2. Let $m \in \mathbb{Z}^+$ denote the total number of optional elements and $s \in \mathbb{Z}^+$ be the maximum number of allowable ones. The probability that the number of optional elements q^* in the obtained optimal structure is more than s has an upper bound, as

$$\mathbb{P}(q^* > s) \leq \sum_{l=s+1}^m \binom{m}{l} \sin^{2l} \left(\frac{\nu^*}{2} \right) \cos^{2(m-l)} \left(\frac{\nu^*}{2} \right). \quad (24)$$

Proof. The initial quantum state is $|\mathbf{0}\rangle^{\otimes m}$. Applying U_R results in the transformed state

$$|\psi\rangle = \sum_{\mathbf{q} \in \{0,1\}^m} \left[\prod_{j=1}^m a(q_j, \nu_j) \right] |\mathbf{q}\rangle, \quad (25)$$

where

$$a(q_j, \nu_j) = \begin{cases} -i \sin \left(\frac{\nu_j}{2} \right) & \text{if } q_j = 1 \\ \cos \left(\frac{\nu_j}{2} \right) & \text{if } q_j = 0 \end{cases}. \quad (26)$$

The probability of obtaining any configuration with l optional elements is then

$$\mathbb{P}(q^* = l) = \sum_{M_l} \left[\prod_{j \in M_l} \sin^2 \left(\frac{\nu_j}{2} \right) \right] \left[\prod_{k \notin M_l} \cos^2 \left(\frac{\nu_k}{2} \right) \right] \quad (l = s + 1, \dots, m), \quad (27)$$

where $M_l \subseteq \{1, \dots, m\}$ such that $|M_l| = l$. The right-hand side of Eq. (27) is a sum over all possible subsets with l integers.

As ν_j increases from 0 to π , $\sin(\nu_j/2)$ increases monotonically. Since ν^* is the upper bound for all ν_j 's,

$$\sum_{M_l} \left[\prod_{j \in M_l} \sin^2 \left(\frac{\nu_j}{2} \right) \right] \left[\prod_{k \notin M_l} \cos^2 \left(\frac{\nu_k}{2} \right) \right] \leq \binom{m}{l} \sin^{2l} \left(\frac{\nu^*}{2} \right) \cos^{2(m-l)} \left(\frac{\nu^*}{2} \right), \quad (28)$$

where $\binom{m}{l} = \frac{m!}{l!(m-l)!}$. Therefore,

$$\mathbb{P}(q^* = l) \leq \binom{m}{l} \sin^{2l} \left(\frac{\nu^*}{2} \right) \cos^{2(m-l)} \left(\frac{\nu^*}{2} \right). \quad (29)$$

and

$$\mathbb{P}(q^* > s) = \sum_{l=s+1}^m \mathbb{P}(q^* = l) \leq \sum_{l=s+1}^m \binom{m}{l} \sin^{2l} \left(\frac{\nu^*}{2} \right) \cos^{2(m-l)} \left(\frac{\nu^*}{2} \right). \quad (30)$$

□

Theorem 2 provides a guidance to set the value of ν^* . Given a probability upper bound of constraint violation, the value of ν^* can be obtained by solving the nonlinear equation in Eq. (24). Some examples are illustrated in Figure 3, where each curve represents the solutions of the nonlinear equation, where the value of ν^* can be identified for the given values of m and s . For a fixed value of m , the upper probability decreases as s increases. It is also observed that the curve corresponding to $s = m$ is constantly zero since there is no volume constraint involved.

4. Success Probability

The success probability of obtaining the optimal solution is derived in this section. The following theorem establishes a lower bound for the probability of gaining extra information from the state of the total ignorance.

Theorem 3 ([38]). Let $\mathbb{H} \otimes \bar{\mathbb{H}}$ be a bipartite Hilbert space and ρ be the density matrix of a quantum state in the subspace \mathbb{H} . Let d_Λ be the number of unique solutions in \mathbb{H} . If there are $l \in \mathbb{Z}^+$ and $c_1 \in \mathbb{R}^+$ such that $d_\Lambda \leq l^{c_1}$, then

$$\begin{aligned} \mathbb{P} \left(\left\| \rho - \frac{1}{d_\Lambda} I \right\|_2^2 \geq e^{-t^2/2} \frac{(1 - d_\Lambda^{-1})}{2} + \mathcal{O}(2^{-l/4}) \right) \\ \geq 1 - \mathcal{O}(2^{-l/2}) \end{aligned} \quad (31)$$

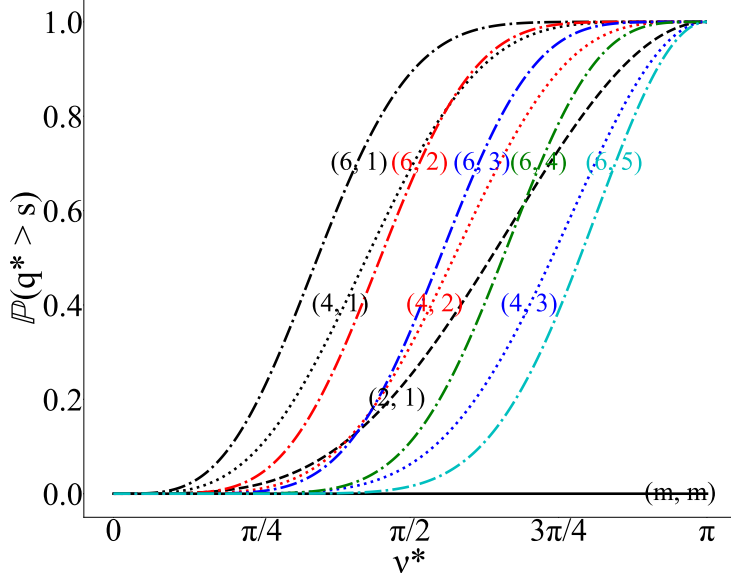


Figure 3: The upper bounds of constraint violation probability for different values of (m, s) . The dashed line corresponds to $m = 2$, the dotted lines correspond to $m = 4$, the dash-dotted lines correspond to $m = 6$, and the solid line corresponds to $s = m$.

where $\mathbb{P}(\cdot)$ denotes probability, $\frac{1}{d_\Lambda}I$ is the state of the total ignorance, $\|A\|_2 = \sqrt{\text{Tr}(A^\dagger A)}$ is the Frobenius norm of matrix A , and the upper bound of computational time t is $\mathcal{O}((\log_2 l)^{1/2})$.

In the proposed VQA, two registers are involved. Therefore, the following corollary is obtained.

Corollary 3.1. Let $\mathbb{H}_q \otimes \mathbb{H}_w$ denote the original Hilbert space, where \mathbb{H}_q is a Hilbert space of m qubits and \mathbb{H}_w is a Hilbert space of n qubits. Suppose that $\mathbb{H}_q \otimes \mathbb{H}_w$ is partitioned into two bipartite subspaces $\mathbb{H}_q \otimes \mathbb{H}_w^{(1)}$ and $\mathbb{H}_q \otimes \mathbb{H}_w^{(2)}$. Let ρ be the density matrix of a quantum state in $\mathbb{H}_q \otimes \mathbb{H}_w^{(1)}$ and d be the number of unique solutions in $\mathbb{H}_w^{(1)}$. If there is $c_2 \in \mathbb{R}^+$ such that $d \leq n^{c_2}$, then

$$\mathbb{P}\left(\left\|\rho - \frac{1}{d2^m}I\right\|_2^2 \leq e^{-t^2/2} \frac{(1 - d^{-1}2^{-m})}{2} + \mathcal{O}(2^{-\frac{m+n}{4}})\right) \leq \mathcal{O}(2^{-(m+n)/2}) \quad (32)$$

where the upper bound of t is $\mathcal{O}([\log_2(m+n)]^{1/2})$.

Proof. From Theorem 3, where $d_\Lambda = d2^m$, we have

$$\mathbb{P}\left(\left\|\rho - \frac{1}{d2^m}I\right\|_2^2 \geq e^{-t^2/2} \frac{(1 - d^{-1}2^{-m})}{2} + \mathcal{O}(2^{-\frac{m+n}{4}})\right) \geq 1 - \mathcal{O}(2^{-(m+n)/2}) \quad (33)$$

and

$$\mathbb{P}\left(\left\|\rho - \frac{1}{d2^m}I\right\|_2^2 \leq e^{-t^2/2} \frac{(1 - d^{-1}2^{-m})}{2} + \mathcal{O}(2^{-\frac{m+n}{4}})\right) \leq \mathcal{O}(2^{-(m+n)/2}). \quad (34)$$

□

The main result about the success probability that the optimal solution is obtained is stated in the following theorem.

Theorem 4. Let $\mathbb{H}_q \otimes \mathbb{H}_w$ denote the original Hilbert space, where \mathbb{H}_q is a Hilbert space of m qubits and \mathbb{H}_w is a Hilbert space of n qubits. Let ρ and ρ^* be the density matrices of an arbitrary quantum state and the target state, respectively. If there exists a C_0 such that

$$0 < C_0 \leq 1 - \frac{(2^{-1} - d^{-1}2^{-m-1})\mathcal{O}(2^{-(m+n)/2}) + \mathcal{O}(2^{-3(m+n)/4})}{e^{-t^2/2}(2^{-1} - d^{-1}2^{-m-1}) + \mathcal{O}(2^{-(m+n)/4})}, \quad (35)$$

then there exists an $\epsilon > 0$ such that

$$\mathbb{P}(\|\rho^* - \rho\|_2^2 \leq \epsilon) \geq 1 - \frac{1 - \frac{(1-C_0)[e^{-t^2/2}(2^{-1}-d^{-1}2^{-m-1})+\mathcal{O}(2^{-(m+n)/4})]}{(2^{-1}-d^{-1}2^{-m-1})+\mathcal{O}(2^{-(m+n)/4})}}{1 - \mathcal{O}(2^{-(m+n)/2})}. \quad (36)$$

Proof. Let $\pi(t)$ be the time-dependent lower bound of information gain, defined as

$$\pi(t) = e^{-t^2/2}(2^{-1} - d^{-1}2^{-m-1}) + \mathcal{O}(2^{-(m+n)/4}), \quad (37)$$

and

$$\Pi(t) = \frac{\pi(t)}{1 - C_0} \quad (38)$$

be the maximum possible information gain of quantum computation. C_0 is regarded as the probability that the information gain at time t is greater than $\pi(t)$. The relationship between $\pi(t)$ and $\Pi(t)$ is illustrated in Figure 4.

Because

$$\mathbb{P}\left(\|\rho^* - \frac{1}{d2^m}I\|_2^2 \geq \pi(t)\right) \geq \mathbb{P}\left(\|\rho - \frac{1}{d2^m}I\|_2^2 \geq \pi(t)\right), \quad (39)$$

we have

$$\mathbb{P}\left(\|\rho^* - \frac{1}{d2^m}I\|_2^2 \geq \pi(t)\right) \geq \mathbb{P}\left(\|\rho - \frac{1}{d2^m}I\|_2^2 \geq \pi(t) + \epsilon\right) \mathbb{P}(\|\rho^* - \rho\|_2^2 \geq \epsilon). \quad (40)$$

Rearrangement of the inequality in Eq. (40) results in

$$\mathbb{P}(\|\rho^* - \rho\|_2^2 \geq \epsilon) \leq \frac{\mathbb{P}\left(\|\rho^* - \frac{1}{d2^m}I\|_2^2 \geq \pi(t)\right)}{\mathbb{P}\left(\|\rho - \frac{1}{d2^m}I\|_2^2 \geq \pi(t) + \epsilon\right)}, \quad (41)$$

where $\Delta t \geq 0$ is a small time step such that $\pi(t - \Delta t) = \pi(t) + \epsilon$. Since $\pi(t)$ and $\Pi(t)$ decrease over time,

$$\mathbb{P}\left(\|\rho^* - \frac{1}{d2^m}I\|_2^2 \geq \pi(t)\right) = 1 - \frac{\pi(t)}{\Pi(t)} \leq 1 - \frac{\pi(t)}{\Pi(0)}. \quad (42)$$

From Corollary 3.1,

$$\begin{aligned} \mathbb{P}(\|\rho^* - \rho\|_2^2 \geq \epsilon) &\leq \frac{1 - \frac{\pi(t)}{\Pi(0)}}{1 - \mathcal{O}(2^{-(m+n)/2})} \\ &= \frac{1 - \frac{(1-C_0)[e^{-t^2/2}(2^{-1}-d^{-1}2^{-m-1})+\mathcal{O}(2^{-(m+n)/4})]}{(2^{-1}-d^{-1}2^{-m-1})+\mathcal{O}(2^{-(m+n)/4})}}{1 - \mathcal{O}(2^{-(m+n)/2})}. \end{aligned} \quad (43)$$

and

$$\mathbb{P}(\|\rho^* - \rho\|_2^2 \leq \epsilon) \geq 1 - \frac{1 - \frac{(1-C_0)[e^{-t^2/2}(2^{-1}-d^{-1}2^{-m-1})+\mathcal{O}(2^{-(m+n)/4})]}{(2^{-1}-d^{-1}2^{-m-1})+\mathcal{O}(2^{-(m+n)/4})}}{1 - \mathcal{O}(2^{-(m+n)/2})}. \quad (44)$$

Note that the conditions in Eq. (35) ensure that the probability of success is between 0 and 1. \square

As the special cases of success probabilities, if $t = 0$,

$$\mathbb{P}(\|\rho^* - \rho\|_2^2 \leq \epsilon) \geq 1 - \frac{C_0}{1 - \mathcal{O}(2^{-(m+n)/2})}. \quad (45)$$

If $t \rightarrow \infty$,

$$\mathbb{P}(\|\rho^* - \rho\|_2^2 \leq \epsilon) \geq 1 - \frac{1 - \frac{(1-C_0)\mathcal{O}(2^{-(m+n)/4})}{(2^{-1}-d^{-1}2^{-m-1})+\mathcal{O}(2^{-(m+n)/4})}}{1 - \mathcal{O}(2^{-(m+n)/2})}. \quad (46)$$

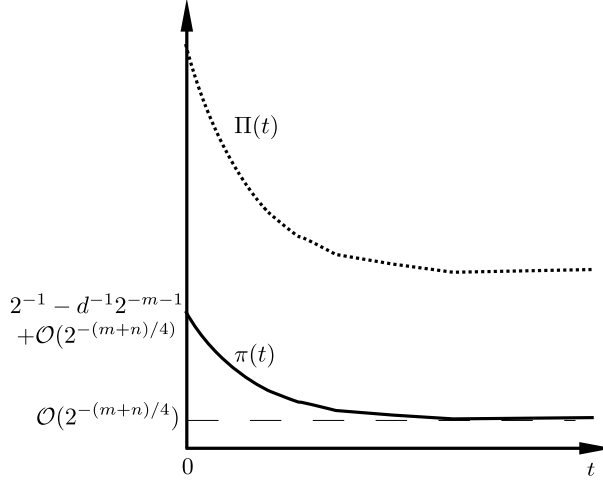


Figure 4: Bounds of information gain

5. Experimental Results

5.1. Compliance Minimization of Truss Structures

The proposed VQA for TO is first demonstrated with three two-dimensional truss structures. The three structures are shown in Figure 5, where the x and y axes represent spatial coordinates in inches. In Figure 5a, truss structure #1 contains three pin supports and a vertical load of 10,000 kilopounds (kips) is applied at node 2. In Figure 5b, truss structure #2 contains four pin supports and a vertical load of 10,000 kips is applied at node 2. In Figure 5c, truss structure #3 contains two pin supports and a vertical load of 1,000 kips is applied at node 5. Each truss consists of a base structure and optional elements. The base structures are illustrated as solid lines, whereas the optional elements are depicted as dashed lines. The cross-sectional areas of elements are 0.1 in^2 in truss structures #1 and #2, whereas the cross-sectional areas are 0.01 in^2 in truss structure #3. The elastic modulus is 29,000 ksi for all truss structures.

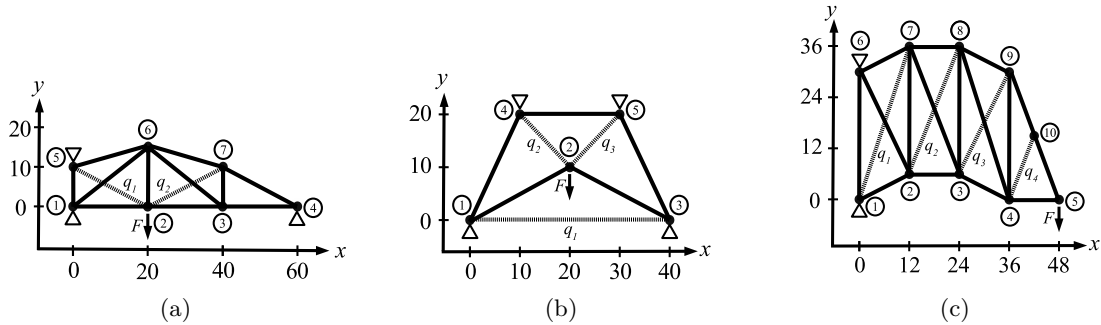


Figure 5: Illustrations of truss structures (a) #1, (b) #2, and (c) #3

Bayesian optimization is performed to find the quantum circuit parameters which result in the optimal configurations. The surrogate model, which is the Gaussian process regressor model with the Matérn covariance kernel, generates a probabilistic distribution of objective functions. The upper confidence bound is used as the acquisition function to search for the optimal parameters.

For each truss structure, the proposed VQA was performed for ten runs to obtain the distributions of the optimal configurations. Each run consists of 50 optimization iterations. The circuit depth is set to $p = 4$. The initial values of Lagrange multipliers λ and μ are both 25 for truss structure #1, 50 for truss structure #2, and 15 for truss structure #3. The multipliers are the largest for truss structure #2 since the number of PDE constraints is the smallest. Both multipliers increase by 1 after each iteration so that feasible solutions are obtained towards the end of optimization.

Two cases of the compliance minimization problem are solved. In the first case, volume constraints are

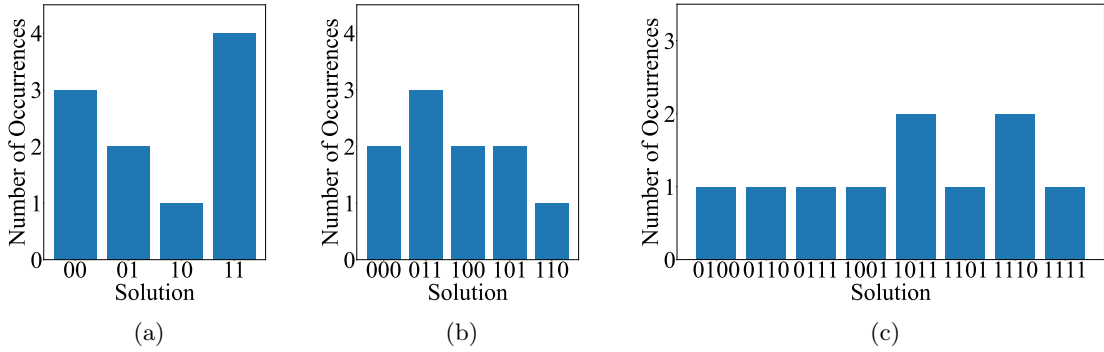


Figure 6: Distributions of the optimal configurations for truss structures (a) #1, (b) #2, and (c) #3 after 50 iterations without volume constraints

not considered. The maximum numbers of optional elements allowed to be included are two for truss structure #1, three for truss structure #2, and four for truss structure #3. The distributions of the optimal configurations without volume constraints are shown in Figure 6. The VQA is able to find the true optimal configurations of all truss structures. In Figure 6a, four out of ten runs result in $q_1q_2 = 11$, which is associated with the minimum strain energy for truss structure #1. In Figure 6b, three runs result in $q_1q_2q_3 = 011$, which is one of the two true optimal configurations for truss structure #2. The other one is $q_1q_2q_3 = 111$. In Figure 6c, two runs result in $q_1q_2q_3q_4 = 1110$, whereas another run results in $q_1q_2q_3q_4 = 1111$, both of which are the true optimal configurations for truss structure #3. Overall, the success probability of finding the true optimal configuration is between 30% and 40%.

In the second case, volume constraints are considered. The maximum numbers of elements allowed to be included are one for truss structures #1 and #2, and two for truss structure #3. To assess the sensitivity of setting the probabilities for violating volume constraints and verify the theoretical upper bound in Theorem 2, the probabilities of violating constraints are also estimated for each structure. Sampling procedures are taken, where eleven values of ν^* , which are multiples of 0.1π ranging from 0 to π , are selected. 100,000 shots are taken for each value on the quantum circuit in Figure 1 without optimizing the parameters. By counting the number of times N_f that a configuration with more than s optional elements are generated out of the 100,000 shots, the constraint violation probability is estimated as $\mathbb{P}(q^* > s) \approx N_f/100000$.

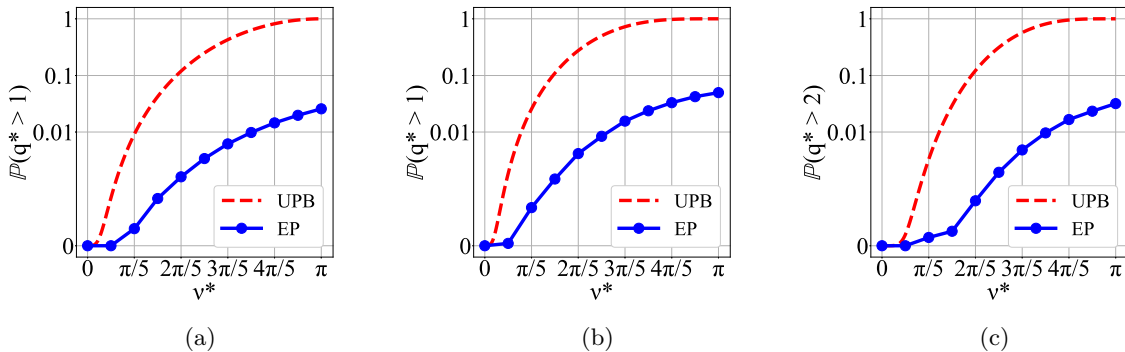


Figure 7: Comparison between upper probability bounds (UPBs) and estimated probabilities (EPs) of violating volume constraints for truss structures (a) #1, (b) #2, and (c) #3.

The estimated constraint violation probabilities and the upper probability bounds from Eq. (24) are shown in Figure 7 for the three truss structures. In all three plots, the upper probability bounds and estimated probabilities increase as ν^* increases from 0 to π . This implies that the volume constraints are not as strictly enforced when ν^* is large. For all values of ν^* , the probability of volume constraint

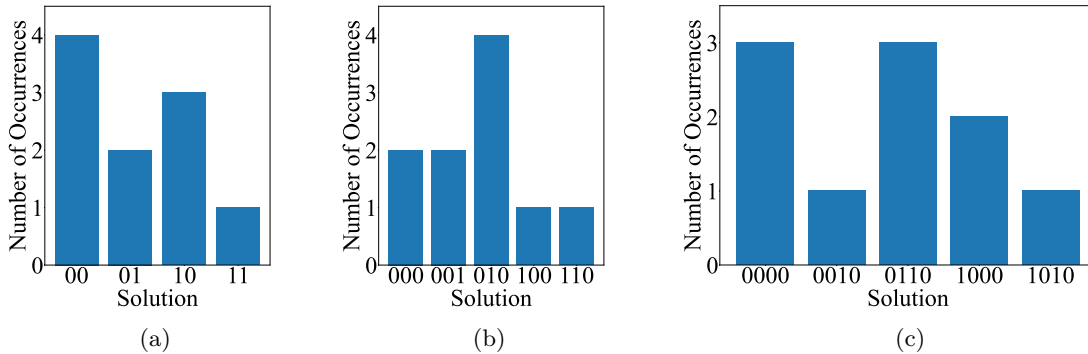


Figure 8: Distributions of the optimal configurations for truss structures (a) #1, (b) #2, and (c) #3 with volume constraints

violation is bounded by the obtained theoretical upper. Without sampling, the theoretical probability upper bounds provide the guidance to choose the values of ν^* in setting the volume constraints. In this example, we set the upper bound of constraint violation probability to be 0.5. Accordingly, ν^* is set to 1.998 for truss structure #1, 1.801 for truss structure #2, and 1.571 for truss structure #3. Notice that although the upper bound of probability is set to be 0.5, the actual probabilities of constraint violation are small. They are 0.0075, 0.0137, and 0.0019 respectively for the three truss structures.

The optimization is performed under the constraint of parameter upper bound ν^* . The distributions of optimal configurations with volume constraints are shown in Figure 8. The VQA is able to find the true optimal configurations for all three structures with success probabilities ranging from 30% to 60%. The true optimal configurations are $q_1q_2 = 10$ for truss structure #1, $q_1q_2q_3 = 001$ and $q_1q_2q_3 = 010$ for truss structure #2, and $q_1q_2q_3q_4 = 0110$ for truss structure #3. In Figure 8a, three of the ten runs result in $q_1q_2 = 10$. In Figure 8b, two runs result in $q_1q_2q_3 = 001$, whereas four runs result in $q_1q_2q_3 = 010$. In Figure 8c, three runs result in $q_1q_2q_3q_4 = 0110$. In addition, among all three distributions of optimal configurations, only one run in Figure 8a results in a configuration which violates the volume constraint. This run results in $q_1q_2 = 11$, which is the true optimal configuration when no volume constraint is enforced.

5.2. Compliance Minimization of MBB Beam

As the second example, the problems of compliance minimization for two MBB beams in Figure 9 are solved. In Figure 9a, beam #1 consists of twelve square elements arranged as a 4×3 rectangular grid. The side length of each element is 2 in. Eight elements, which are depicted as solid gray regions, comprise the base structure. The other four elements, which are depicted as striped regions, are optional elements. Four roller supports and two pin supports are located along the left and bottom edges, respectively. A vertical load of 200,000 kips is applied at node 17. In Figure 9b, the twelve square elements in beam #2, each with a side length of 2 in, are arranged as a 3×4 rectangular grid. Six elements comprise the base structure, whereas the other six elements are optional. Similar to beam #1, four roller supports and two pin supports are located along the left and bottom edges. A vertical load of 200,000 kips is applied at node 16.

For beam #1, one volume constraint and one topological constraint are considered. For the volume constraint, the maximum number of optional elements allowed to be included is two. For the topological constraint, q_4 must be zero if q_2 and q_3 are both zero. The implementation of this topological constraint is shown in Figure 2. Beam #2 involves one volume constraint and two topological constraints. For the volume constraint, the maximum number of optional elements is two. For the first topological constraint, q_5 must be zero if q_2 and q_4 are both zeros. For the second topological constraint, q_6 must be zero if q_3 and q_5 are both zeros.

Similar to the previous truss problems, the upper bound of volume constraint violation is set to be 0.5 for the MBB problems. For the illustration purpose, the probabilities of violation and the upper bounds are

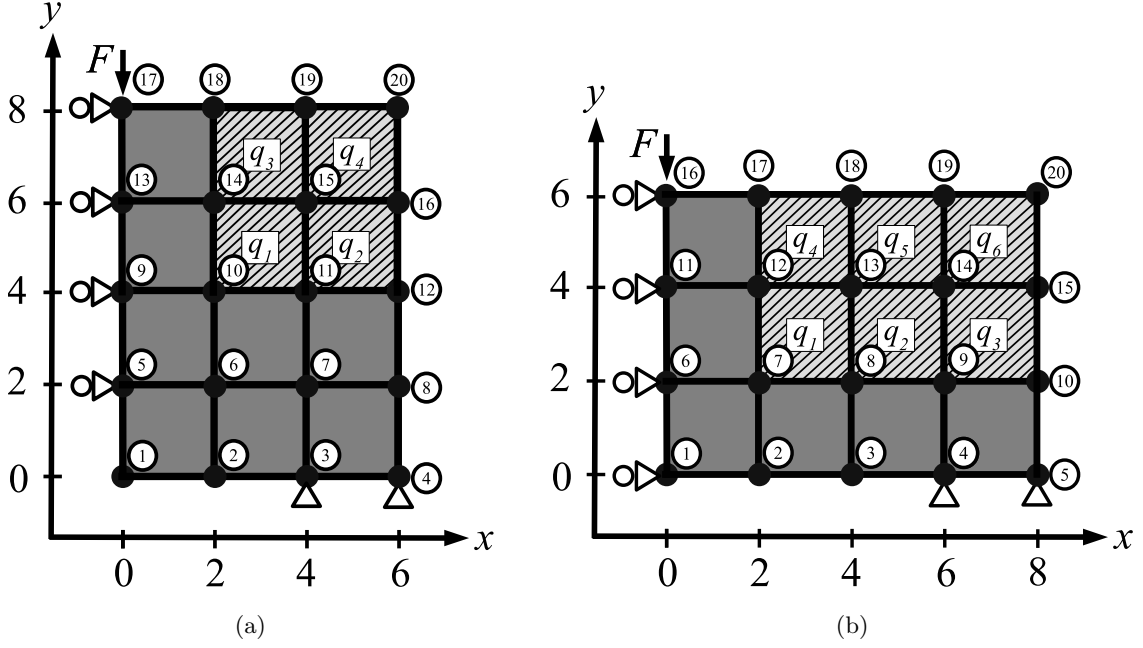


Figure 9: Illustrations of MBB beams (a) #1 and (b) #2

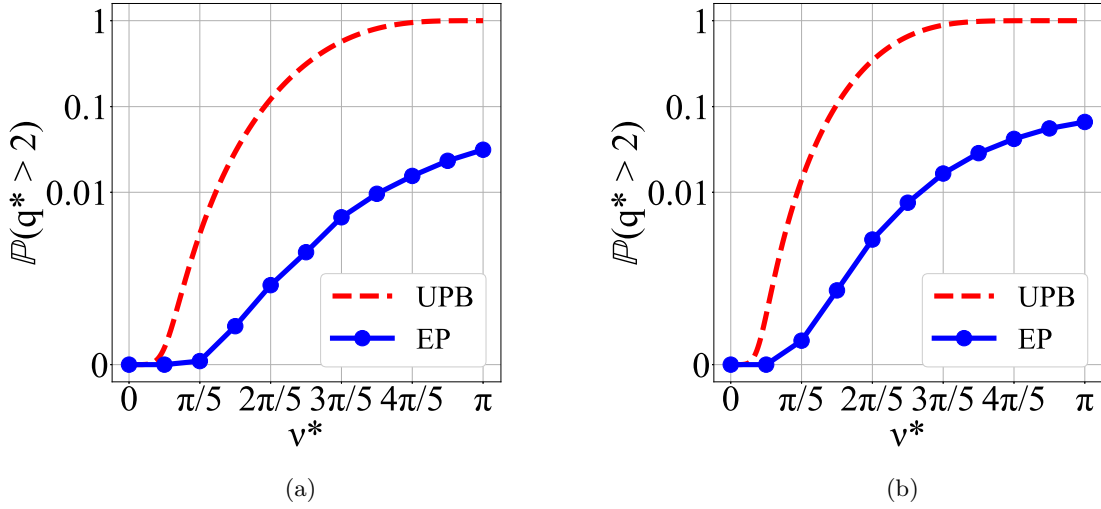


Figure 10: Comparison between upper probability bounds (UPBs) and estimated probabilities (EPs) of violating volume constraints for MBB beams (a) #1 and (b) #2

similarly compared in Figure 10. Based on the probability upper bound of 0.5, the values of parameter upper bounds ν^* 's are set to be 1.571 for MBB beam #1 and 1.413 for beam #2. Accordingly, the values of ξ in the quantum circuit are -1.571 for beam #1 and -1.413 for beam #2.

Ten runs of the VQA were performed, where each run consists of 50 optimization iterations. The initial values of λ and μ are 0.5 and 5, respectively. The values of the Lagrange multipliers in the beam examples are larger than those in the truss examples since it is more difficult to solve the PDE constraints. The value of λ increases by 0.1 after each iteration for both beams. The value of μ increases by 0.5 and 0.1 for beams #1 and #2, respectively. The change in μ is smaller for beam #2 since the number of possible solutions is larger than that of beam #1.

Figure 11 shows the distributions of optimal configurations. In Figure 11a, four out of the runs result in $q_1q_2q_3q_4 = 1010$, which is the true optimal configuration for beam #1 with volume constraints. In Figure 11b, four runs result in $q_1q_2q_3q_4q_5q_6 = 110000$, which is the true optimal feasible configuration

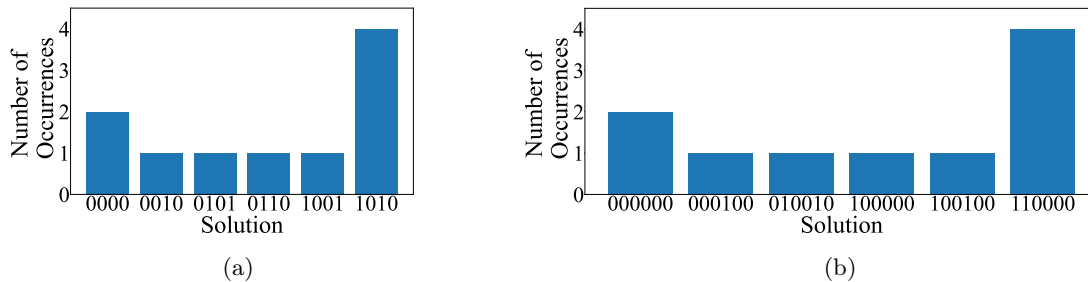


Figure 11: Distributions of the optimal configurations for MBB beams (a) #1 and (b) #2 after 50 iterations

for beam #2 with volume constraints. Overall, the success probability is 40%. It is also observed that none of the optimal configurations contain more than two optional elements. Therefore, the VQA with the selected values of ν^* can enforce the volume constraints when the number of optional elements is between four and six.

6. Discussions and Conclusions

In this paper, a new variational quantum algorithm for constrained topology optimization is proposed to find the optimal material configuration and solve the PDE constraints simultaneously. The single-loop optimization is achieved by constructing the controlled problem Hamiltonian operators so that the two registers are entangled. The number of gates scales with a factor of $\mathcal{O}(nv^2 [\log_2(2^{1/2}\|Q^{(\cdot)}\|_{\max})])$. This factor depends on the sparsity of stiffness matrices, the degrees of element connectivity, and the number of qubits. Typically, the stiffness matrices are sparse and the degrees of element connectivity are small for two- and three-dimensional structures. Therefore, the number of gates scales linearly with respect to the number of qubits.

The topological and volume constraints in the optimization problems are also incorporated in the proposed VQA. The probability upper bound of volume constraints is derived to provide the guidance for setting the upper bound of the rotation gate parameters. The advantage of this encoding scheme for volume constraints is its simplicity where the constraints on VQA parameters can be easily enforced on the classical computer side. Encoding the topological constraints, however, is more complex because circuits need to be customized with the entanglement between qubits.

The success probability of the algorithm is also analyzed. The lower bound, or certainty about the success probability of obtaining the optimal solution, exponentially decreases as the computational time increases. The lower bound of the success probability quickly approaches the limit that is dependent on the number of qubits, which indicates that the level of uncertainty increases along time. Therefore, the circuit breadth and depth need to be properly controlled and optimized to improve the efficiency of the VQA.

The proposed VQA is demonstrated with compliance minimization problems involving three truss structure and two MBB beams. Across all five examples, the VQA is implemented with at most 12 qubits and 22 Hermitian operators in the problem Hamiltonian. Solving TO problems with larger structures requires more qubits and deeper circuits. Future work will focus on reducing the number of qubits and the circuit depth of the VQA. Reducing the depth is particularly important to reduce the amount of time for running the circuit and to improve the success probability. The success probability can also be improved by updating the quantum circuit architecture during the optimization iterations. Based on real-time compilation, the gate composition and circuit depth can be modified in order to improve the efficiency of sampling.

References

- [1] Martin Philip Bendsøe and Ole Sigmund. *Topology optimization: theory, methods, and applications*. Springer Science & Business Media, 2013.

- [2] Fridolin Okkels and Henrik Bruus. Scaling behavior of optimally structured catalytic microfluidic reactors. *Physical Review E*, 75(1):016301, 2007.
- [3] Zin Lin, Adi Pick, Marko Lončar, and Alejandro W. Rodriguez. Enhanced spontaneous emission at third-order Dirac exceptional points in inverse-designed photonic crystals. *Physical Review Letters*, 117(10):107402, 2016.
- [4] Rasmus E. Christiansen, Fengwen Wang, and Ole Sigmund. Topological insulators by topology optimization. *Physical Review Letters*, 122(23):234502, 2019.
- [5] Garuda Fujii and Youhei Akimoto. DC electric cloak concentrator via topology optimization. *Physical Review E*, 102(3):033308, 2020.
- [6] Zi-xiang Xu, Hao Gao, Yu-jiang Ding, Jing Yang, Bin Liang, and Jian-chun Cheng. Topology-optimized omnidirectional broadband acoustic ventilation barrier. *Physical Review Applied*, 14(5):054016, 2020.
- [7] Takao Hagishita and Makoto Ohsaki. Topology optimization of trusses by growing ground structure method. *Structural and Multidisciplinary Optimization*, 37:377–393, 2009.
- [8] José Pedro Blasques and Mathias Stolpe. Multi-material topology optimization of laminated composite beam cross sections. *Composite Structures*, 94(11):3278–3289, 2012.
- [9] Yan Wang. Simulating stochastic diffusions by quantum walks. In *International Design Engineering Technical Conferences and Computers and Information in Engineering Conference*, volume 55898, page V03BT03A053. American Society of Mechanical Engineers, 2013.
- [10] Yan Wang. Accelerating stochastic dynamics simulation with continuous-time quantum walks. In *International Design Engineering Technical Conferences and Computers and Information in Engineering Conference*, volume 50183, page V006T09A053. American Society of Mechanical Engineers, 2016.
- [11] Yan Wang. Global optimization with quantum walk enhanced Grover search. In *International Design Engineering Technical Conferences and Computers and Information in Engineering Conference*, volume 46322, page V02BT03A027. American Society of Mechanical Engineers, 2014.
- [12] Yan Wang, Jungin E. Kim, and Krishnan Suresh. Opportunities and challenges of quantum computing for engineering optimization. *Journal of Computing and Information Science in Engineering*, 23(6):060817, 2023.
- [13] Bela Bauer, Sergey Bravyi, Mario Motta, and Garnet Kin-Lic Chan. Quantum algorithms for quantum chemistry and quantum materials science. *Chemical Reviews*, 120(22):12685–12717, 2020.
- [14] Vera von Burg, Guang Hao Low, Thomas Häner, Damian S. Steiger, Markus Reiher, Martin Roetteler, and Matthias Troyer. Quantum computing enhanced computational catalysis. *Physical Review Research*, 3(3):033055, 2021.
- [15] Yudong Cao, Jhonathan Romero, and Alán Aspuru-Guzik. Potential of quantum computing for drug discovery. *IBM Journal of Research and Development*, 62(6):6:1–6:20, 2018.
- [16] Satoshi Morita and Hidetoshi Nishimori. Mathematical foundation of quantum annealing. *Journal of Mathematical Physics*, 49(12):125210, 2008.
- [17] Tameem Albash and Daniel A. Lidar. Adiabatic quantum computation. *Reviews of Modern Physics*, 90(1):015002, 2018.
- [18] Zisheng Ye, Xiaoping Qian, and Wenxiao Pan. Quantum topology optimization via quantum annealing. *IEEE Transactions on Quantum Engineering*, 4:3100515, 2023.
- [19] Rio Honda, Katsuhiko Endo, Taichi Kaji, Yudai Suzuki, Yoshiki Matsuda, Shu Tanaka, and Mayu Muramatsu. Development of optimization method for truss structure by quantum annealing. *Scientific Reports*, 14(1):13872, 2024.
- [20] Edward Farhi, Jeffrey Goldstone, and Sam Gutmann. A quantum approximate optimization algorithm. *arXiv preprint arXiv:1411.4028*, 2014.

- [21] Stuart Hadfield, Zhihui Wang, Bryan O’Gorman, Eleanor G. Rieffel, Davide Venturelli, and Rupak Biswas. From the quantum approximate optimization algorithm to a quantum alternating operator ansatz. *Algorithms*, 12(2):34, 2019.
- [22] Alberto Peruzzo, Jarrod McClean, Peter Shadbolt, Man-Hong Yung, Xiao-Qi Zhou, Peter J. Love, Alán Aspuru-Guzik, and Jeremy L. O’Brien. A variational eigenvalue solver on a photonic quantum processor. *Nature Communications*, 5(1):4213, 2014.
- [23] Jungin E. Kim and Yan Wang. Topology optimization with quantum approximate Bayesian optimization algorithm. In *ASME International Design Engineering Technical Conferences and Computers and Information in Engineering Conference*, volume 87318, page V03BT03A034, 2023.
- [24] Jungin E. Kim and Yan Wang. Quantum approximate Bayesian optimization algorithms with two mixers and uncertainty quantification. *IEEE Transactions on Quantum Engineering*, 4:3102817, 2023.
- [25] Yuki Sato, Ruho Kondo, Satoshi Koide, and Seiji Kajita. Quantum topology optimization of ground structures for near-term devices. In *2023 IEEE International Conference on Quantum Computing and Engineering (QCE)*, volume 1, pages 168–176. IEEE, 2023.
- [26] Itay Hen and Marcelo S. Sarandy. Driver Hamiltonians for constrained optimization in quantum annealing. *Physical Review A*, 93(6):062312, 2016.
- [27] Samuel Fernández-Lorenzo, Diego Porras, and Juan José García-Ripoll. Hybrid quantum–classical optimization with cardinality constraints and applications to finance. *Quantum Science and Technology*, 6(3):034010, 2021.
- [28] Hristo N. Djidjev. Logical qubit implementation for quantum annealing: augmented Lagrangian approach. *Quantum Science and Technology*, 8(3):035013, 2023.
- [29] Alejandro Montañez Barrera, Dennis Willsch, Alberto Maldonado-Romo, and Kristel Michielsen. Unbalanced penalization: a new approach to encode inequality constraints of combinatorial problems for quantum optimization algorithms. *Quantum Science and Technology*, 9(2):025022, 2024.
- [30] Zhihui Wang, Nicholas C. Rubin, Jason M. Dominy, and Eleanor G. Rieffel. XY mixers: analytical and numerical results for the quantum alternating operator ansatz. *Physical Review A*, 101(1):012320, 2020.
- [31] Stuart Hadfield, Tad Hogg, and Eleanor G. Rieffel. Analytical framework for quantum alternating operator ansätze. *Quantum Science and Technology*, 8(1):015017, 2022.
- [32] Hannes Leipold and Federico M. Spedalieri. Constructing driver Hamiltonians for optimization problems with linear constraints. *Quantum Science and Technology*, 7(1):015013, 2021.
- [33] Yan Wang. A quantum approximate Bayesian optimization algorithm for continuous problems. In *IIE Annual Conference. Proceedings*, pages 235–240. Institute of Industrial and Systems Engineers (IISE), 2021.
- [34] Dengke Qu, Edric Matwiejew, Kunkun Wang, Jingbo Wang, and Peng Xue. Experimental implementation of quantum-walk-based portfolio optimization. *Quantum Science and Technology*, 9(2):025014, 2024.
- [35] Pablo Díez-Valle, Jorge Luis-Hita, Senaida Hernández-Santana, Fernando Martínez-García, Álvaro Díaz-Fernández, Eva Andrés, Juan José García-Ripoll, Escolástico Sánchez-Martínez, and Diego Porras. Multiobjective variational quantum optimization for constrained problems: an application to cash handling. *Quantum Science and Technology*, 8(4):045009, 2023.
- [36] Masuo Suzuki. Generalized Trotter’s formula and systematic approximants of exponential operators and inner derivations with applications to many-body problems. *Communications in Mathematical Physics*, 51(2):183–190, 1976.
- [37] William M. Kirby and Peter J. Love. Variational quantum eigensolvers for sparse Hamiltonians. *Physical Review Letters*, 127(11):110503, 2021.
- [38] Lorenzo Leone, Salvatore F. E. Oliviero, Lukasz Cincio, and M. Cerezo. On the practical usefulness of the hardware efficient ansatz. *Quantum*, 8:1395, 2024.